A time discretisation scheme based on integrated radial basis functions for heat transfer and fluid flow problems

T.T.V. Le[a], N. Mai-Duy[a,*], K. Le-Cao[b] and T. Tran-Cong[a]
[a]Computational Engineering and Science Research Centre,
School of Mechanical and Electrical Engineering,
University of Southern Queensland, Toowoomba, QLD 4350, Australia
[b]Department of Mechanical Engineering, Faculty of Engineering,
National University of Singapore, Singapore

Submitted to *Numerical Heat Transfer, Part B*, April/2018; revised, August/2018
Short title: An integrated-RBF-based time discretisation scheme

ABSTRACT This paper reports a new numerical procedure, which is based on integrated radial basis functions (IRBFs) and Cartesian grids, for solving time-dependent differential problems that can be defined on non-rectangular domains. For space discretisations, compact five-point IRBF stencils [Journal of Computational Physics, vol. 235, pp. 302-321, 2013] are utilised. For time discretisations, a two-point IRBF scheme is proposed, where the time derivative is approximated in terms of not only nodal function values at the current and previous time levels but also nodal derivative values at the previous time level. This allows functions other than a linear one to also be captured well on a time step. The use of the RBF width as an additional parameter to enhance the approximation quality with respect to time is also explored. Various kinds of test problems of heat transfer and fluid flows are conducted to demonstrate attractiveness of the present compact

*Corresponding author: E-mail nam.mai-duy@usq.edu.au, Telephone +61 7 46312748, Fax +61 7 46312529

approximations.

Keywords: time discretisations; integrated radial basis functions; compact approximations; heat transfer and fluid flows.

NOMENCLATURE

c	integration constant	t	time variable
CM	convergence measure	T	temperature
D	side length of outer square cylinder	u, v	x and y components of velocity
D_i	diameter of inner cylinder	w	RBF weight
g	gravitational acceleration	W	width of rectangular channel
G	radial basis function (RBF)	$\mathbf{x}$	spatial variable
h	water depth	x, y	coordinates
H	mean water depth	β	thermal expansion coefficient
$\mathcal{I}/Q$	spatial/temporal integrated RBF	β_s	spatial RBF width
k	time level	β_t	temporal RBF width
l	thermal conductivity	γ	thermal diffusivity
L	length of rectangular channel	ϵ	tolerance
m	number of RBFs/nodal points	ζ	water surface elevation
MAE	maximum of absolute error	ν	kinematic viscosity
n	normal direction	ψ	stream function
n_{ip}	number of interior points	ω	vorticity
n_t	total number of time steps	**Subscripts**	
Ne	discrete relative L_2 error	b	boundary value
Nu	Nusselt number	$[\alpha]$	a component of $\mathbf{x}$
Pr	Prandtl number	**Superscripts**	
Ra	Rayleigh number	e	exact solution
$RMSE$	root-mean-square error	(q)	order of an IRBF scheme

1 Introduction

Over the last twenty five years, radial basis functions (RBFs), which possess the property of universal approximation, have been used with great success to solve different types of differential problems in applied mathematics, science and engineering [2,3]. RBF methods can work with a

set of unstructured discrete points and they have the ability to produce highly accurate results. Approximations of the field variable and its derivatives in terms of RBFs can be constructed through the differential process (DRBF) [4] or the integral process (IRBF) [5]. The latter was originally developed to (i) avoid the reduction in convergence rate caused by differentiation; and (ii) provide an effective way of implementing multiple boundary conditions. For global RBF methods, a function is approximated using all RBFs over the domain. It is known that the global RBF system matrix is fully populated and its condition number grows rapidly with increasing number of nodes. To circumvent this problem, there have been several attempts in the development of local RBF methods, where only a small subregion, namely the influence domain, is activated for the construction of the RBF approximations at a point. Works reported include [6-14]. Local methods lead to a sparse and better-conditioned system matrix. However, their solution accuracy is observed to significantly deteriorate. Compact local RBF methods have been developed. In these methods, the approximations involve nodal values of not only the field variable but also its derivatives [10,15,16], which allows both a high level of the solution accuracy and sparseness of the system matrix to be achieved together. In using RBFs to solve differential problems, the time derivative terms are usually discretised by means of low-order finite differences (FDs), for which small time steps are typically required. In this study, we propose a discretisation procedure based on compact IRBF stencils only for time-dependent heat and fluid flow problems in two dimensions. An IRBF stencil is of 2 nodes and 5 nodes for time and space discretisations, respectively.

The remainder of the paper is organised as follows. Section 2 gives a brief review of integrated RBFs and their compact forms for space discretisations. Section 3 describes a new compact two-point approximation based on IRBFs for time discretisations, and a numerical procedure based on compact IRBF stencils only for solving time-dependent differential problems. Numerical results are presented in Section 4. Section 5 concludes the paper.

2 Integrated RBFs

Our proposed numerical procedure is based on integrated RBFs. Some relevant schemes of IRBFs are briefly reviewed here for the sake of completeness.

2.1 Original scheme

Highest-order derivatives of the field variable f in the ordinary/partial differential equations (ODEs/PDEs) are decomposed into RBFs, from which expressions for lower-order derivatives and the variable itself are derived through integration

$$\frac{\partial^q f(\mathbf{x})}{\partial \alpha^q} = \sum_{i=1}^{m} w_{[\alpha]i} G_i(\mathbf{x}) = \sum_{i=1}^{m} w_{[\alpha]i} \mathcal{I}_{[\alpha]i}^{(q)}(\mathbf{x}), \tag{1}$$

$$\frac{\partial^{q-1} f(\mathbf{x})}{\partial \alpha^{q-1}} = \sum_{i=1}^{m} w_{[\alpha]i} \mathcal{I}_{[\alpha]i}^{(q-1)}(\mathbf{x}) + c_{[\alpha]1}, \tag{2}$$

$$\cdots \qquad \cdots \qquad \cdots$$

$$f(\mathbf{x}) = \sum_{i=1}^{m} w_{[\alpha]i} \mathcal{I}_{[\alpha]i}^{(0)}(\mathbf{x}) + \frac{\alpha^{q-1}}{(q-1)!} c_{[\alpha]1} + \frac{\alpha^{q-2}}{(q-2)!} c_{[\alpha]2} + ... + c_{[\alpha]q}, \tag{3}$$

where α is a component of the independent spatial variable $\mathbf{x}$, the subscript $[\alpha]$ is used to differentiate the IRBF approximations with respect to each coordinate, m the number of RBFs, $G_i(\mathbf{x})$ the RBF, $\mathcal{I}_{[\alpha]i}^{(q-1)}(\mathbf{x}) = \int \mathcal{I}_{[\alpha]i}^{(q)}(\mathbf{x}) d\alpha, ..., \mathcal{I}_{[\alpha]i}^{(0)}(\mathbf{x}) = \int \mathcal{I}_{[\alpha]i}^{(1)}(\mathbf{x}) d\alpha$, $(w_{[\alpha]1}, w_{[\alpha]2}, ..., w_{[\alpha]m})$ the coefficients, and $(c_{[\alpha]1}, c_{[\alpha]2}, ..., c_{[\alpha]q})$ the integration constants that are functions of variables other than α. Making use of (1)-(3) and point collocation, one can transform the ODE/PDE into a set of algebraic equations, from which the coefficients and integration constants can be acquired [5].

2.2 Compact approximation scheme

IRBFs have been used to construct the approximations on Cartesian grids representing a domain of rectangular/non-rectangular shape [1,17]. Advantages of this approach lie in its economic preprocessing. Consider a domain that is embedded in a Cartesian grid as shown in Figure 1. Grid points outside the domain (external points) together with the internal points that fall very close - within a small distance - to the boundary are removed. The remaining grid points are taken to be the interior nodes. The boundary nodes are points that are generated by the intersection of the grid lines with the boundaries. In this work, second order differential problems are considered and for a space discretisation, a 5-point stencil associated with node (i, j) is employed with nodes being locally numbered from left to right and from bottom to top ($(i, j) \equiv 3$) (Figure 1). Derivatives of the dependent variable f in the x and y directions are approximated by IRBFs along the lines defined by $1-3-5$ and $2-3-4$, respectively. One can utilise the integration constants in the IRBF formulation to incorporate some nodal derivative values in the approximations. In the x direction, evaluation of (3) at (x_1, x_3, x_5) and of (1) at (x_1, x_5) using $q = 2$ result in

$$\widetilde{f} = \underbrace{\begin{bmatrix} \mathbf{I} \\ \mathbf{B} \end{bmatrix}}_{\mathcal{C}} \widetilde{w}, \tag{4}$$

where

$$\widetilde{f} = \begin{pmatrix} f_1 & f_3 & f_5 & \frac{\partial^2 f_1}{\partial x^2} & \frac{\partial^2 f_5}{\partial x^2} \end{pmatrix}^T, \tag{5}$$

$$\widetilde{w} = \begin{pmatrix} w_{[x]1} & w_{[x]3} & w_{[x]5} & c_{[x]1} & c_{[x]2} \end{pmatrix}^T, \tag{6}$$

$$\mathbf{I} = \begin{bmatrix} \mathcal{I}^{(0)}_{[x]1}(x_1) & \mathcal{I}^{(0)}_{[x]3}(x_1) & \mathcal{I}^{(0)}_{[x]5}(x_1) & x_1 & 1 \\ \mathcal{I}^{(0)}_{[x]1}(x_3) & \mathcal{I}^{(0)}_{[x]3}(x_3) & \mathcal{I}^{(0)}_{[x]5}(x_3) & x_3 & 1 \\ \mathcal{I}^{(0)}_{[x]1}(x_5) & \mathcal{I}^{(0)}_{[x]3}(x_5) & \mathcal{I}^{(0)}_{[x]5}(x_5) & x_5 & 1 \end{bmatrix},$$

and

$$\mathbf{B} = \begin{bmatrix} \mathcal{I}^{(2)}_{[x]1}(x_1) & \mathcal{I}^{(2)}_{[x]3}(x_1) & \mathcal{I}^{(2)}_{[x]5}(x_1) & 0 & 0 \\ \mathcal{I}^{(2)}_{[x]1}(x_5) & \mathcal{I}^{(2)}_{[x]3}(x_5) & \mathcal{I}^{(2)}_{[x]5}(x_5) & 0 & 0 \end{bmatrix}.$$

The system (4) can be solved for the unknown coefficient vector $\widetilde{w}$, resulting in

$$\widetilde{w} = \mathcal{C}^{-1}\widetilde{f}, \tag{7}$$

where $\mathcal{C}^{-1}$ is the inverse of $\mathcal{C}$.

Expressions for computing f and its derivatives at point x, where $x_1 \leq x \leq x_5$, can then be obtained by substituting (7) into (3), (2) and (1) with $q = 2$

$$f(x) = \begin{bmatrix} \mathcal{I}^{(0)}_{[x]1}(x) & \mathcal{I}^{(0)}_{[x]3}(x) & \mathcal{I}^{(0)}_{[x]5}(x) & x & 1 \end{bmatrix} \mathcal{C}^{-1}\widetilde{f}, \tag{8}$$

$$\frac{\partial f(x)}{\partial x} = \begin{bmatrix} \mathcal{I}^{(1)}_{[x]1}(x) & \mathcal{I}^{(1)}_{[x]3}(x) & \mathcal{I}^{(1)}_{[x]5}(x) & 1 & 0 \end{bmatrix} \mathcal{C}^{-1}\widetilde{f}, \tag{9}$$

$$\frac{\partial^2 f(x)}{\partial x^2} = \begin{bmatrix} \mathcal{I}^{(2)}_{[x]1}(x) & \mathcal{I}^{(2)}_{[x]3}(x) & \mathcal{I}^{(2)}_{[x]5}(x) & 0 & 0 \end{bmatrix} \mathcal{C}^{-1}\widetilde{f}, \tag{10}$$

which can be rewritten as

$$f(x) = \phi_1(x) f_1 + \phi_3(x) f_3 + \phi_5(x) f_5 + \bar{\phi}_1(x) \frac{\partial^2 f_1}{\partial x^2} + \bar{\phi}_5(x) \frac{\partial^2 f_5}{\partial x^2}, \tag{11}$$

$$\frac{\partial f(x)}{\partial x} = \frac{d\phi_1(x)}{dx} f_1 + \frac{d\phi_3(x)}{dx} f_3 + \frac{d\phi_5(x)}{dx} f_5 + \frac{d\bar{\phi}_1(x)}{dx} \frac{\partial^2 f_1}{\partial x^2} + \frac{d\bar{\phi}_5(x)}{dx} \frac{\partial^2 f_5}{\partial x^2}, \tag{12}$$

$$\frac{\partial^2 f(x)}{\partial x^2} = \frac{d^2\phi_1(x)}{dx^2} f_1 + \frac{d^2\phi_3(x)}{dx^2} f_3 + \frac{d^2\phi_5(x)}{dx^2} f_5 + \frac{d^2\bar{\phi}_1(x)}{dx^2} \frac{\partial^2 f_1}{\partial x^2} + \frac{d^2\bar{\phi}_5(x)}{dx^2} \frac{\partial^2 f_5}{\partial x^2}. \tag{13}$$

At $x = x_3$, they reduce to

$$\frac{\partial f_3}{\partial x} = \mu_1 f_1 + \mu_3 f_3 + \mu_5 f_5 + \bar{\mu}_1 \frac{\partial^2 f_1}{\partial x^2} + \bar{\mu}_5 \frac{\partial^2 f_5}{\partial x^2}, \tag{14}$$

$$\frac{\partial^2 f_3}{\partial x^2} = \eta_1 f_1 + \eta_3 f_3 + \eta_5 f_5 + \bar{\eta}_1 \frac{\partial^2 f_1}{\partial x^2} + \bar{\eta}_5 \frac{\partial^2 f_5}{\partial x^2}, \tag{15}$$

where $\mu_1 = d\phi_1(x_3)/dx$, $\mu_3 = d\phi_3(x_3)/dx$, $\mu_5 = d\phi_5(x_3)/dx$, $\bar{\mu}_1 = d\bar{\phi}_1(x_3)/dx$, $\bar{\mu}_5 = d\bar{\phi}_5(x_3)/dx$, $\eta_1 = d^2\phi_1(x_3)/dx^2$, $\eta_3 = d^2\phi_3(x_3)/dx^2$, $\eta_5 = d^2\phi_5(x_3)/dx^2$, $\bar{\eta}_1 = d^2\bar{\phi}_1(x_3)/dx^2$, and $\bar{\eta}_5 = d^2\bar{\phi}_5(x_3)/dx^2$.

Similarly, on the line $2-3-4$, one obtains

$$\frac{\partial f_3}{\partial y} = \nu_2 f_2 + \nu_3 f_3 + \nu_4 f_4 + \bar{\nu}_2 \frac{\partial^2 f_2}{\partial y^2} + \bar{\nu}_4 \frac{\partial^2 f_4}{\partial y^2}, \tag{16}$$

$$\frac{\partial^2 f_3}{\partial y^2} = \theta_2 f_2 + \theta_3 f_3 + \theta_4 f_4 + \bar{\theta}_2 \frac{\partial^2 f_2}{\partial y^2} + \bar{\theta}_4 \frac{\partial^2 f_4}{\partial y^2}. \tag{17}$$

With nodal derivative values being approximated in the form of (14), (15), (16) and (17), collocating the ODE/PDE at grid nodes will lead to a sparse system matrix, of which each row has only 5 entries. Note that the nodal derivative values on the right hand side of (14)-(17) can be treated as known quantities.

3 Proposed IRBF-based method

3.1 An IRBF-based two-point time discretisation scheme

In the proposed scheme, the variation of the dependent variable f on each interval (time step) defined by two points, t_{k-1} and t_k, is represented by IRBFs. Without loss of generality, we consider

the following parabolic PDE

$$\frac{\partial f}{\partial t}(x,y,t) - \left(\frac{\partial^2 f}{\partial x^2}(x,y,t) + \frac{\partial^2 f}{\partial y^2}(x,y,t)\right) = b(x,y,t), \tag{18}$$

defined on the domain Ω and subjected to initial values and boundary conditions. In (18), b is a given function (the source). Using the conventional finite difference method, one can reduce the PDE to

$$\frac{f_{ij}^k - f_{ij}^{k-1}}{\Delta t} - \lambda\left(\frac{\partial^2 f_{ij}^k}{\partial x^2} + \frac{\partial^2 f_{ij}^k}{\partial y^2}\right) - (1-\lambda)\left(\frac{\partial^2 f_{ij}^{k-1}}{\partial x^2} + \frac{\partial^2 f_{ij}^{k-1}}{\partial y^2}\right) = b_{ij}^{k-1+\lambda}, \tag{19}$$

where the subscript ij is used to denote the function at grid node (i,j), the superscript k the function evaluated at the time level t_k, $\Delta t = t_k - t_{k-1}$, and $\lambda = 0$ and $\lambda = 1$ correspond to the explicit and implicit schemes, respectively. Our goal here is to construct an approximating function from RBFs, which can capture a curved line rather than a straight line over two nodes t_{k-1} and t_k. It is proposed that the first-order derivative of f with respect to t is decomposed into RBFs

$$\frac{\partial f(t)}{\partial t} = w_{k-1}G_{k-1}(t) + w_k G_k(t), \tag{20}$$

where, for the multiquadric (MQ) case, $G_{k-1}(t) = \sqrt{(t-t_{k-1})^2 + a_{k-1}^2}$ and $G_k(t) = \sqrt{(t-t_k)^2 + a_k^2}$ in which a_{k-1} and a_k are the MQ widths. Expression for computing f is then derived as

$$f(t) = w_{k-1}Q_{k-1}(t) + w_k Q_k(t) + c_1, \tag{21}$$

where $Q_{k-1}(t) = \int G_{k-1}(t)\,dt$, $Q_k(t) = \int G_k(t)\,dt$, and c_1 is the constant of integration. It should be emphasised that function f in (21) is defined with three coefficients (i.e. w_{k-1}, w_k and c_1) over two nodal points (i.e. t_{k-1} and t_k). This allows one to add one extra equation in the system of converting the RBF space into the physical space. Here we use this extra equation to include the

derivative value of f evaluated at the previous time level. Its details are as follows

$$\begin{pmatrix} f^k \\ f^{k-1} \\ \frac{\partial f}{\partial t}^{k-1} \end{pmatrix} = \mathcal{C}_t \begin{pmatrix} w_{k-1} \\ w_k \\ c_1 \end{pmatrix}, \tag{22}$$

where $\mathcal{C}_t$ is the conversion matrix defined as

$$\mathcal{C}_t = \begin{pmatrix} Q_{k-1}(t_k) & Q_k(t_k) & 1 \\ Q_{k-1}(t_{k-1}) & Q_k(t_{k-1}) & 1 \\ G_{k-1}(t_{k-1}) & G_k(t_{k-1}) & 0 \end{pmatrix}.$$

Making use of (22), the three coefficients can be expressed in terms of the nodal variable values and the derivative value at the previous time level

$$\begin{pmatrix} w_{k-1} \\ w_k \\ c_1 \end{pmatrix} = \mathcal{C}_t^{-1} \begin{pmatrix} f^k \\ f^{k-1} \\ \frac{\partial f}{\partial t}^{k-1} \end{pmatrix}. \tag{23}$$

Expression for computing the first-order derivative at the current time level thus becomes

$$\frac{\partial f}{\partial t}^k = \begin{bmatrix} G_{k-1}(t_k) & G_k(t_k) & 0 \end{bmatrix} \begin{pmatrix} w_{k-1} \\ w_k \\ c_1 \end{pmatrix}, \tag{24}$$

$$= \begin{bmatrix} G_{k-1}(t_k) & G_k(t_k) & 0 \end{bmatrix} \mathcal{C}_t{}^{-1} \begin{pmatrix} f^k \\ f^{k-1} \\ \frac{\partial f}{\partial t}^{k-1} \end{pmatrix}, \tag{25}$$

which can be rewritten as

$$\frac{\partial f}{\partial t}^k = D_1 f^k + D_2 f^{k-1} + D_3 \dot{f}^{k-1}, \tag{26}$$

with D_1, D_2, D_3 being computed from the RBFs and the inverse of $\mathcal{C}_t$ - they are known values. The time derivative term is now expressed in term of values of f at t_{k-1} and t_k (i.e. f^{k-1} and f^k) and its time derivative at t_{k-1} (i.e. $\frac{\partial f}{\partial t}^{k-1}$ or simply $\dot{f}^{k-1}$). An alternative to the discretisation

scheme (19) is

$$D_1 {f_{ij}}^k + D_2 {f_{ij}}^{k-1} + D_3 \dot{f}_{ij}^{k-1} - \lambda \left({\frac{\partial^2 f_{ij}}{\partial x^2}}^k + {\frac{\partial^2 f_{ij}}{\partial y^2}}^k \right) - (1-\lambda) \left({\frac{\partial^2 f_{ij}}{\partial x^2}}^{k-1} + {\frac{\partial^2 f_{ij}}{\partial y^2}}^{k-1} \right) = b_{ij}^{k-1+\lambda}. \tag{27}$$

As shown in Figure 2, a function approximated by IRBFs on a time step can be of nonlinear form. It is expected that larger time steps can be used in simulating time-dependent differential problems, where the slope of the solution varies between time levels.

3.2 An IRBF-based space-time discretisation scheme

The combination of the proposed compact 2-point stencil for time and the presented compact 5-point stencil for space results in a numerical procedure, which is based on IRBFs only, for solving time-dependent differential problems. With the explicit scheme (i.e. $\lambda = 0$), the calculation is based on the solution of (15) and (17) evaluated at the previous time level

$$-\bar{\eta}_1 {\frac{\partial^2 f_1}{\partial x^2}}^{k-1} + {\frac{\partial^2 f_3}{\partial x^2}}^{k-1} - \bar{\eta}_5 {\frac{\partial^2 f_5}{\partial x^2}}^{k-1} = \eta_1 f_1^{k-1} + \eta_3 f_3^{k-1} + \eta_5 f_5^{k-1}, \tag{28}$$

$$-\bar{\theta}_2 {\frac{\partial^2 f_2}{\partial y^2}}^{k-1} + {\frac{\partial^2 f_3}{\partial y^2}}^{k-1} - \bar{\theta}_4 {\frac{\partial^2 f_4}{\partial y^2}}^{k-1} = \theta_2 {f_2}^{k-1} + \theta_3 {f_3}^{k-1} + \theta_4 {f_4}^{k-1}. \tag{29}$$

It can be seen that these two equations for nodal derivative values lead to systems of tridiagonal algebraic equations on the x and y grid lines that can be solved efficiently by the Thomas algorithm. Note that nodal values of second derivatives on the boundary can be calculated using any 1D approximation scheme on their associated grid lines. In some cases such as rectangular domains, instead of using 1D approximations, one can directly derive these values from the governing equation and the given boundary conditions.

With the implicit schemes (i.e. $0 < \lambda \leq 1$), there are three unknowns at an interior grid node (i.e.

values of f and its second derivatives in the x and y directions). A set of three algebraic equations needed for each node consists of the two equations (15) and (17) evaluated at the current time level, i.e.

$$-\bar{\eta}_1 \frac{\partial^2 f_1}{\partial x^2}^k + \frac{\partial^2 f_3}{\partial x^2}^k - \bar{\eta}_5 \frac{\partial^2 f_5}{\partial x^2}^k = \eta_1 f_1^k + \eta_3 f_3^k + \eta_5 f_5^k, \tag{30}$$

$$-\bar{\theta}_2 \frac{\partial^2 f_2}{\partial y^2}^k + \frac{\partial^2 f_3}{\partial y^2}^k - \bar{\theta}_4 \frac{\partial^2 f_4}{\partial y^2}^k = \theta_2 f_2{}^k + \theta_3 f_3{}^k + \theta_4 f_4{}^k. \tag{31}$$

and the equation directly derived from the PDE (i.e. equation (27)). It is possible to combine these three equations to form two tridiagonal algebraic equations through the implicit elimination approach as discussed in [1].

4 Numerical examples

In this study, IRBFs are implemented with the multiquadric (MQ) function in the form of

$$G_i(\alpha) = \sqrt{(\alpha - c_i)^2 + a_i^2}, \tag{32}$$

where c_i and a_i are the centre and the width of the ith MQ, respectively and α can be x or y in the spatial approximation and t in the temporal approximation. The MQ width is simply chosen according to the relation

$$a_i = \beta_s d_i \quad \text{for space,} \tag{33}$$

$$a_i = \beta_t \Delta t \quad \text{for time,} \tag{34}$$

where β_s and β_t are positive values, d_i the smallest distance between the centre c_i and its neighbours, and Δt the time step. Different types of time-dependent problems are chosen to study the performance of the proposed numerical procedure. The first three examples are concerned with

the heat transfer, convection-diffusion and shallow water equations, of which the analytic solutions are available. In the fourth (last) example, the proposed method is applied for the simulation of natural convection flows in the region between a square outer cylinder and a circular inner cylinder. Some standard finite difference schemes are also employed where appropriate to provide the base for the evaluation of accuracy of the proposed time stencil. Note that a distinguishing feature of the RBF solution is that its accuracy can be controlled not only by the grid size/time step but also by the RBF width. For all numerical examples, the problem domain is simply discretised using a uniform Cartesian grid. The value of d_i in (33) thus becomes a grid size. In the case of curved boundaries, a distance to the boundary used for the removing of interior nodes is chosen as $d_i/8$. When the analytic solution is available, the numerical error is measured in the form of

1. Discrete relative L_2 norm

$$Ne = \frac{\sqrt{\sum_{i=1}^{m}(f_i^e - f_i)^2}}{\sqrt{\sum_{i=1}^{m}(f_i^e)^2}}, \tag{35}$$

2. Root-mean-square error (RMSE)

$$RMSE = \sqrt{\frac{1}{n_t}\sum_{i=1}^{n_t}(f_i^e - f_i)^2}, \tag{36}$$

3. Maximum of absolute error (MAE)

$$MAE = \|f_i^e - f_i\|_{\max}, \tag{37}$$

where m is the number of nodal points, n_t the number of time steps, and f^e and f respectively denote the exact and approximate solutions. In the last example, the flow is considered to reach the steady state when the following condition is satisfied

$$CM = \frac{\sqrt{\sum_{i=1}^{n_{ip}}\left(f_i^k - f_i^{k-1}\right)^2}}{\sqrt{\sum_{i=1}^{n_{ip}}\left(f_i^k\right)^2}} < \epsilon, \tag{38}$$

where n_{ip} is the number of interior points, k the time level, f the stream function and ϵ the tolerance. In this study, ϵ is taken to be 10^{-12}.

4.1 Example 1: Parabolic PDEs

4.1.1 One dimensional space

The proposed method is first verified in the following PDE

$$\frac{\partial f}{\partial t}(x,t) = \frac{\partial^2 f}{\partial^2 x}(x,t) + b(x,t), \quad 0 \le x \le 1, \tag{39}$$

with $b(x,t) = 50xe^{50t}$. Its exact solution is given by

$$f^e(x,y,t) = xe^{50t}, \tag{40}$$

from which one can derive the initial values and Dirichlet boundary conditions. As shown in Figure 3, function f grows very quickly with time.

To assess accuracy of the time discretisation only, we approximate the time derivative term in (39) explicitly using the forward differences and the proposed compact time stencils, and employ the same spatial approximation for the two schemes. The second derivative $\partial^2 f/\partial^2 x$ is approximated by compact IRBF stencils on a set of 10 nodes with $\beta_s = 3.5$. Figure 4 displays the solution error by the two schemes at $\Delta t = 10^{-3}$. It can be seen that the IRBF solution is much more accurate than the FD one. To achieve the same accuracy level of the IRBF time scheme, as shown in Figure 5, the FD time scheme needs a much smaller time step (i.e. $\Delta t = 10^{-6}$). The obtained results of this example demonstrate that the proposed compact time stencil has the ability to work with relatively large time steps for a given accuracy.

4.1.2 Two dimensional space

The PDE to be considered here is in the form of

$$\frac{\partial f}{\partial t}(x,y,t) - \left(\frac{\partial^2 f}{\partial x^2}(x,y,t) + \frac{\partial^2 f}{\partial y^2}(x,y,t)\right) = 3e^t \sin(x)\sin(y), \tag{41}$$

The exact solution is given by

$$f^e(x,y,t) = \sin(x)\sin(y)e^t. \tag{42}$$

This function grows exponentially with time and thus provides a good test for the proposed compact time stencil. The initial values and Dirichlet boundary conditions can be derived from (42).

We consider two types of domains, a unit square and a multiply-connected domain that is a region lying between a unit square and a circle of radius 0.2. The explicit approach is employed to obtain the numerical solutions of (41).

For the unit square, to examine accuracy of the proposed compact time stencils, we also implement the forward differences. These two time approximation schemes are employed with the same time step of 10^{-3} and the same spatial approximation that is based on central differences on a grid density of 10×10. Figure 6 shows that a much improved accuracy is obtained with the proposed scheme ($\beta_t = 12$). It is noted that the accuracy is computed over the whole spatial domain. As also shown in the figure, a further improvement can be achieved by replacing the spatial central differences with the compact 5-node IRBF stencils using $\beta_s = 3.5$. For the multi-connected domain, because of its non-rectangular shape, we only employ the compact 5-node IRBF stencils for the spatial approximation. The obtained results on a grid density of 22×22 and with $\Delta t = 10^{-4}$ are displayed in Figure 7. Again, it can be seen that results by the proposed compact time stencil

are more accurate than those by the forward differences.

4.2 Example 2: Convection-Diffusion equations

The proposed method is further verified with the convection-diffusion equations in one and two dimensional space.

4.2.1 One dimensional space

Consider the following equation

$$\frac{\partial f}{\partial t}(x,t) + f(x,t)\frac{\partial f}{\partial x}(x,t) = \frac{\partial^2 f}{\partial x^2}(x,t) + 2\sin(x)e^t + \sin(x)\cos(x)e^{2t}, \tag{43}$$

on an interval $[0,1]$ with the initial and boundary conditions

$$f(x,0) = \sin(x), \tag{44}$$

$$f(0,t) = 0, \tag{45}$$

$$f(1,t) = \sin(1)e^t. \tag{46}$$

The exact solution to this problem can be verified to be $f^e(x,t) = \sin(x)e^t$.

We employ compact 3-point IRBF stencils on a grid of 10 nodes with $\beta_s = 3.5$ for the spatial approximation, and compact 2-point IRBF stencils for the temporal approximation. Attention here is given to the effects of the RBF width in the time domain on the solution accuracy. The obtained results at a time step of 10^{-3} are shown in Figure 8. Results by the forward differences are also included for comparison purposes. It can be seen that better accuracy can be achieved by changing the RBF width. The effect of increasing β_t here is similar to the effect of reducing

Δt; however, changing β_t does not lead to any increase in computational cost.

4.2.2 Two dimensional space

An unsteady convection-diffusion equation in two dimensional space for a variable f can be expressed as

$$\frac{\partial f}{\partial t}(x,y,t) + c_x \frac{\partial f}{\partial x}(x,y,t) + c_y \frac{\partial f}{\partial y}(x,y,t) = d_x \frac{\partial^2 f}{\partial x^2}(x,y,t) + d_y \frac{\partial^2 f}{\partial y^2}(x,y,t) + b(x,y,t). \quad (47)$$

Here, we choose $c_x = c_y = 0.01$, $d_x = d_y = 1$ and

$$b(x,y,t) = 3\sin(x)\sin(y)\, r + 0.01r\left(\cos(x)\sin(y) + \cos(y)\sin(x)\right).$$

The domain of interest is of $[0,1] \times [0,1]$ and the initial and boundary conditions are given by

$$u(x,y,0) = \sin(x)\sin(y), \quad (48)$$

$$u(0,y,t) = u(x,0,t) = 0, \quad (49)$$

$$u(1,y,t) = \sin(1)\sin(y)\, r, \quad (50)$$

$$u(x,1,t) = \sin(x)\sin(1)\, r, \quad (51)$$

where

$$r = 1 + t + \frac{t^2}{2} + \frac{t^3}{6} + \frac{t^4}{24} + \frac{t^5}{120}.$$

This problem has the following exact solution

$$f^e(x,t) = \sin(x)\sin(y)r. \quad (52)$$

The problem domain is represented by a Cartesian grid of 10×10. Other parameters employed are $\beta_s = 3.5$ and $\Delta t = 10^{-3}$. As shown in Figure 9, with the same spatial approximation employed,

the proposed compact time scheme outperforms the conventional forward differences. Similar remarks to the case of one dimensional space can also be made here. In particular, the solution accuracy can be enhanced by changing the MQ width (β_t) without any additional computational cost.

4.3 Example 3: Shallow water equations (SWEs)

RBF methods have been applied to solve the shallow water equations (SWEs). Their solutions are reported using the global MQ approximation [18-20], compactly supported radial-basis function (CSRBF) [21] and local radial-basis-function differential quadrature (LRBFDQ) [22] methods. In these works, the time derivative term is approximated by conventional finite-difference schemes. For SWEs, there are two dependent variables, namely the water height in the z direction, denoted by h, and the velocity vector in the $x-y$ plane, denoted by (u, v). They are functions of space $\mathbf{x}$ and time t.

The continuity and momentum SWEs can be linearised as follows

$$\frac{\partial h}{\partial t}(x,y,t) + H\left(\frac{\partial u}{\partial x}(x,y,t) + \frac{\partial v}{\partial y}(x,y,t)\right) = 0, \tag{53}$$

$$\frac{\partial u}{\partial t}(x,y,t) + g\frac{\partial h}{\partial x}(x,y,t) = 0, \tag{54}$$

$$\frac{\partial v}{\partial t}(x,y,t) + g\frac{\partial h}{\partial y}(x,y,t) = 0, \tag{55}$$

where $g = 9.81\ m/s^2$. For convenience, the water depth h can be regarded as the sum of the mean water depth H and the water surface elevation ζ.

Consider a rectangular channel of length $L = 872\ km$ and width $W = 50\ km$ with the fluid being water as shown in Figure 10. The mean water depth is $H = 20\ m$.

The boundary condition for the water surface elevation is specified as

$$\zeta(x, y, t) = \zeta_0 \cos at,$$

at $x = 0$, $0 \leq y \leq W$, $\zeta_0 = 1\ m$ and $a = 1.45444 \times 10^{-4} s^{-1}$, while the land boundary conditions are

$$u(x, y, t) = 0,$$

at $x = L$, $0 \leq y \leq W$ and

$$u(x, y, t) = 0,$$

at $y = 0$ and $y = W$, $0 \leq x \leq L$. The initial conditions are prescribed as

$$u(x, y, t = 0) = 0, \tag{56}$$

$$v(x, y, t = 0) = 0, \tag{57}$$

$$\zeta(x, y, t = 0) = \zeta_0 \cos\left(\frac{a}{\sqrt{gH}}(L - x)\right) / \cos\left(\frac{a}{\sqrt{gH}} L\right). \tag{58}$$

This fluid flow problem has the following exact solution

$$\zeta(x, y, t) = \zeta_0 \cos\left(\frac{a}{\sqrt{gH}}(L - x)\right) \cos at / \cos\left(\frac{a}{\sqrt{gH}} L\right), \tag{59}$$

$$u(x, y, t) = -\zeta_0 \sqrt{\frac{g}{H}} \sin\left(\frac{a}{\sqrt{gH}}(L - x)\right) \sin at / \cos\left(\frac{a}{\sqrt{gH}} L\right), \tag{60}$$

$$v(x, y, t) = 0. \tag{61}$$

As in [22], for comparison purposes, we also discretise the fluid domain using a set of 205 collocation points and employ a time step of 30 s. The results obtained from proposed method are shown in Table 1 together with those by the global-MQ method [20], CSRBF method [21] and LRBFDQ method employed with 9 (R_9) and 13 (R_{13}) local nodes per approximation [22]. The temporal term is discretised by the Taylor method with second-order accuracy for the global-MQ and CSRBF

methods, and full-implicit FD scheme for LRBFDQ. All the numerical results displayed in Table 1 are computed at $t = 43200\ s$ and at three particular points 102, 103, and 104 which are located at the center of the basin (Figure 10). The units of water depth and velocity used are cm and cm/s, respectively. Errors for the water height and velocities are also measured by means of $RMSE$ and MAE defined in (36) and (37), respectively. It can be seen that the proposed method yields the most accurate results. Figure 11 shows the water free surfaces at two time levels ($t = 14400\ s$ and $t = 43200\ s$) and the IRBF results look feasible when compared to the analytic solutions.

4.4 Example 4: Buoyancy-driven flows

In this example, natural convection between a heated inner circular cylinder of diameter D_i and a cooled square enclosure of side length D is considered (Figure 12). This problem has been investigated with both experimental and numerical works. The latter was conducted by a variety of numerical techniques such as the finite-difference methods [23,24], finite-element methods [25-27], finite-volume methods [28,29], RBF-based methods [30], lattice Boltzmann methods [31,32] and spectral methods [33-35]. The governing equations can be written in terms of the stream function (ψ), vorticity (ω) and temperature (T)

$$\nabla^2 \psi = \omega, \tag{62}$$

$$\frac{\partial \omega}{\partial t} + (\mathbf{u} \cdot \boldsymbol{\nabla})\omega = \sqrt{\frac{Pr}{Ra}} \nabla^2 \omega - \frac{\partial T}{\partial x}, \tag{63}$$

$$\frac{\partial T}{\partial t} + (\mathbf{u} \cdot \boldsymbol{\nabla})T = \frac{1}{\sqrt{RaPr}} \nabla^2 T, \tag{64}$$

where $\mathbf{u}$ is the velocity vector ($u = \partial\psi/\partial y$ and $v = -\partial\psi/\partial x$), and Pr and Ra the Prandtl and Rayleigh numbers defined as $Pr = \nu/\gamma$ and $Ra = \beta g \Delta T D^3/\gamma\nu$, in which ν is the kinematic viscosity, γ the thermal diffusivity, β the thermal expansion coefficient and g the gravity.

We employ an aspect ratio of $D/D_i = 2.5$, $Pr = 0.71$ and $Ra = \{10^4, 5 \times 10^4, 10^5, 5 \times 10^5, 10^6\}$. Non-slip boundary conditions and the symmetry of flow about the vertical centreline lead to $\psi = 0$ and $\partial\psi/\partial n = 0$ (n - the normal direction) on the inner and outer boundaries. Following [36], we derive boundary conditions for equation (63). The values of the vorticity at the boundary nodes on the x and y grid lines can be computed by

$$\omega_b = [1 + (\frac{y}{x})^2]\frac{\partial^2\psi_b}{\partial x^2}, \tag{65}$$

$$\omega_b = [1 + (\frac{x}{y})^2]\frac{\partial^2\psi_b}{\partial y^2}, \tag{66}$$

respectively. The boundary conditions for (64) are $T = 1$ and $T = 0$ on the inner and outer surfaces, respectively.

The fluid domain is discretised using a grid density of 30×30. The three equations (62)-(64) must be solved simultaneously; an iterative scheme, where the convection terms are treated explicitly, is employed to obtain a convergent solution with time. When the difference between two successive stream function fields can be negligible, the flow is considered to reach the steady state. Numerical experiments indicate that the proposed compact time stencil can work with larger time step than the conventional finite difference scheme, leading to a faster convergence as shown in Figure 13. The obtained velocity vector field and contour plots of the temperature are displayed in Figure 14, where 21 contour lines are used with their levels varying linearly between the minimum and maximum values. They look feasible when compared to existing results by other methods.

One important result of this type of flow is the local heat transfer coefficient defined as [29]

$$\Theta = -l\frac{\partial T}{\partial n}, \tag{67}$$

where l is the thermal conductivity. The average Nusselt number (the ratio of the temperature

gradient at the wall to a reference temperature gradient) is computed by

$$Nu = \frac{\overline{\Theta}}{l}, \tag{68}$$

where $\overline{\Theta} = -\oint \frac{\partial T}{\partial n} ds$. Since the computational domain in [29] is taken as one-half of the physical domain, values of Nu in the present work are divided by 2 for comparison purposes. Results concerning Nu for several values of Ra are shown in Table 2 along with those reported in [29,36,37]. It can be seen that they are in good agreement. Especially, for highly nonlinear solutions (e.g. $Ra = 10^6$), the result obtained from the proposed method is very close to that of the differential quadrature method [37] but without the need of doing coordinate transformation.

5 Concluding remarks

In this study, a new approximation scheme for the time derivative term is proposed. The time stencil is based on 2 nodes over which integrated RBFs are employed to represent the field variable. In addition, apart from two nodal values of the field variable, its derivative value at the first node of the stencil is also included the approximation. When compared to conventional first-order finite differences, numerical results indicate that larger time steps can be employed with the proposed time discretisation scheme. In this work, we combine the proposed time scheme with the space compact 5-point IRBF stencils, resulting in a numerical procedure, based on compact IRBF approximations only, for solving parabolic PDEs. The method is applied to simulate shallow water flows in large-scale domains and natural convection flows in multiply-connected domains, and produces accurate results using relatively large time steps.

Acknowledgements This research is supported by Computational Engineering and Science Research Centre (CESRC), University of Southern Queensland, and Institute of Applied

References

1. N. Mai-Duy, and T. Tran-Cong, A compact five-point stencil based on integrated RBFs for 2D second-order differential problems, *Journal of Computational Physics*, vol. 235, pp. 302-321, 2013.

2. G.E. Fasshauer, *Meshfree Approximation Methods with Matlab*, World Scientific, New Jersey, 2007.

3. W. Chen, Z.J. Fu, and C.S. Chen, *Recent Advances in Radial Basis Function Collocation Methods*, Springer, Berlin, 2014.

4. E.J. Kansa, Multiquadrics-A scattered data approximation scheme with applications to computational fluid-dynamics-II solutions to parabolic, hyperbolic and elliptic partial differential equations, *Computers and Mathematics with Applications*, vol. 19, no. 8, pp. 147-161, 1990.

5. N. Mai-Duy, and T. Tran-Cong, Numerical solution of differential equations using multiquadric radial basis function networks, *Neural Networks*, vol. 14, pp. 185-199, 2001.

6. J. Waters, and D.W. Pepper, Global versus localized RBF meshless methods for solving incompressible fluid flow with heat transfer, *Numerical Heat Transfer, Part B: Fundamentals*, vol.68, no. 3, pp. 185-203, 2015.

7. Z.H. Wang, Z. Huang, W. Zhang, and G. Xi, A meshless local radial basis function method for two-dimensional incompressible Navier-Stokes equations, *Numerical Heat Transfer, Part B: Fundamentals*, vol. 67, no. 4, pp. 320-337, 2015.

8. E. Divo, and A.J. Kassab, An efficient localized radial basis function meshless method for fluid flow and conjugate heat transfer, *Journal of Heat Transfer*, vol. 129, no. 2, pp. 124-136, 2007.

9. N. Mai-Duy, and T. Tran-Cong, A Cartesian-grid discretisation scheme based on local integrated RBFNs for two-dimensional elliptic problems, *CMES: Computer Modeling in Engineering and Sciences*, vol. 51, no. 3, pp. 213-238, 2009.

10. N. Mai-Duy, and T. Tran-Cong, Compact local integrated-RBF approximations for second-order elliptic differential problems, *Journal of Computational Physics*, vol. 230, no. 12, pp. 4772-4794, 2011.

11. C. Shu, H. Ding, and K. Yeo, Local radial basis function-based differential quadrature method and its application to solve two-dimensional incompressible Navier-Stokes equations, *Computer Methods in Applied Mechanics and Engineering*, vol. 192, no. 7-8, pp. 941-954, 2003.

12. E. Skouras, G. Bourantas, V. Loukopoulos, and G. Nikiforidis, Truly meshless localized type techniques for the steady-state heat conduction problems for isotropic and functionally graded materials, *Engineering Analysis with Boundary Elements*, vol. 35, no. 3, pp. 452-464, 2011.

13. N. Thai-Quang, K. Le-Cao, N. Mai-Duy, C.D. Tran, and T. Tran-Cong, A numerical scheme based on compact integrated-RBFs and AdamsBashforth/CrankNicolson algorithms for diffusion and unsteady fluid flow problems, *Engineering Analysis with Boundary Elements*, vol. 37, no. 12, pp. 1653-1667, 2013.

14. Y.L. Wu, and G.R. Liu, A meshfree formulation of local radial point interpolation method (LRPIM) for incompressible flow simulation, *Computational Mechanics*, vol. 30, no. 5-6, pp. 355-365, 2003.

15. C.M.T. Tien, N. Thai-Quang, N. Mai-Duy, C.D. Tran, and T. Tran-Cong, A three-point coupled compact integrated RBF scheme for second-order differential problems, *CMES: Computer Modeling in Engineering and Sciences*, vol. 104, no. 6, pp. 425-469, 2015.

16. G.B. Wright, and B. Fornberg, Scattered node compact finite difference-type formulas generated from radial basis functions, *Journal of Computational Physics*, vol. 212, no. 1, pp. 99-123, 2006.

17. N. Mai-Duy, and T. Tran-Cong, A Cartesian-grid collocation method based on radial basis function networks for solving PDEs in irregular domains, *Numerical Methods for Partial Differential Equations*, vol. 23, no. 5, pp. 1192-1210, 2007.

18. Y.C. Hon, K.F. Cheung, X.Z. Mao, and E.J. Kansa, Multiquadric solution for shallow water equations, *Journal of Hydraulic Engineering*, vol. 125, no. 5, pp. 524-533, 1999.

19. D.L. Young, S.C. Jane, C.Y. Lin, C.L. Chiu, and K.C. Chen, Solutions of 2D and 3D Stokes laws using multiquadrics method, *Engineering Analysis with Boundary Elements*, vol. 28, no. 10, pp. 1233-1243, 2004.

20. D.L. Young, C.S. Chen, and T.K. Wong, Solution of Maxwell's equations using the MQ method, *Computers, Materials & Continua*, vol. 2, pp. 267-76, 2005.

21. S.M. Wong, Y.C. Hon, and M.A. Golberg, Compactly supported radial basis functions for shallow water equations, *Applied Mathematics and Computation*, vol. 127, no. 1, pp. 79-101, 2002.

22. C.P. Sun, D.L. Young, L.H. Shen, T.F. Chen, and C.C. Hsian, Application of localized meshless methods to 2D shallow water equation problems, *Engineering Analysis with Boundary Elements*, vol. 37, no. 11, pp. 1339-1350, 2013.

23. G. De Vahl Davis, Natural convection of air in a square cavity: a bench mark numerical solution, *International Journal for Numerical Methods in Fluids*, vol. 3, no. 3, pp. 249-264, 1983.

24. T.H. Kuehn, and R.J. Goldstein, An experimental and theoretical study of natural convection in the annulus between horizontal concentric cylinders, *Journal of Fluid Mechanics*, vol. 74, no. 4, pp. 695-719, 1976.

25. M.T. Manzari, An explicit finite element algorithm for convection heat transfer problems, *International Journal Numerical Methods for Heat and Fluid Flow*, vol. 9, no. 8, pp. 860-877, 1999.

26. H. Sammouda, A. Belghith, and C. Surry, Finite element simulation of transient natural convection of low-Prandtl-number fluids in heated cavity, *International Journal of Numerical Methods for Heat and Fluid Flow*, vol. 9, no. 5, pp. 612-624, 1999.

27. L. Jin, and H. Shen, Projection-and characteristic-based operator-splitting simulation of mixed convection flow coupling heat transfer and fluid flow in a lid-driven square cavity, *Numerical Heat Transfer, Part B: Fundamentals*, vol. 70, no. 4, pp. 354-371, 2016.

28. E.K. Glakpe, C.B. Watkins Jr, and J.N. Cannon, Constant heat flux solutions for natural convection between concentric and eccentric horizontal cylinders, *Numerical Heat Transfer, Part A: Applications*, vol. 10, no. 3, pp. 279-295, 1986.

29. F. Moukalled, and S. Acharya, Natural convection in the annulus between concentric horizontal circular and square cylinders, *Journal of Thermophysics and Heat Transfer*, vol. 10, no. 3, pp. 524-531, 1996.

30. B. Sarler, J. Perko, and C.S. Chen, Radial basis function collocation method solution of natural convection in porous media, *International Journal of Numerical Methods for Heat and Fluid Flow*, vol. 14, no. 2, pp. 187-212, 2004.

31. Y. Wang, C. Shu, C. J. Teo, and L. M. Yang, A fractional-step lattice Boltzmann flux solver for axisymmetric thermal flows, *Numerical Heat Transfer, Part B: Fundamentals*, vol. 69, no. 2, pp. 111-129, 2016.

32. A. J. Ahrar, and M. H. Djavareshkian, Novel hybrid lattice Boltzmann technique with TVD characteristics for simulation of heat transfer and entropy generations of MHD and natural convection in a cavity, *Numerical Heat Transfer, Part B: Fundamentals*, vol. 72, no. 6, pp. 431-449, 2017.

33. P. Le Quere, Accurate solutions to the square thermally driven cavity at high Rayleigh number, *Computers and Fluids*, vol. 20, no. 1, pp. 29-41, 1991.

34. C. Shu, Application of differential quadrature method to simulate natural convection in a concentric annulus, *International Journal for Numerical Methods in Fluids*, vol. 30, no. 8, pp. 977-993, 1999.

35. Z. Wang, Z. Huang, W. Zhang and G. Xi, A multidomain chebyshev pseudo-spectral method for fluid flow and heat transfer from square cylinders, *Numerical Heat Transfer, Part B: Fundamentals*, vol. 68, no. 3, pp. 224-238, 2015.

36. K. Le-Cao, N. Mai-Duy, and T. Tran-Cong, An effective integrated-RBFN Cartesian-grid discretization for the stream function vorticity temperature formulation in nonrectangular domains, *Numerical Heat Transfer, Part B: Fundamentals*, vol. 55, no. 6, pp. 480-502, 2009.

37. C. Shu, and Y.D. Zhu, Efficient computation of natural convection in a concentric annulus between an outer square cylinder and an inner circular cylinder, *International Journal for Numerical Methods in Fluids*, vol. 38, pp. 429-445, 2002.

Table 1: Example 3, shallow water flows: Comparison of numerical errors at three nodes 102, 103, and 104 between the proposed method and the LRBFDQ, CSRBF and global MQ methods.

Numerical error	Water depth (h) (cm)			Velocity (u) (cm/s)		
	102	103	104	102	103	104
Proposed method						
$RMSE$	0.007	0.007	0.0072	0.0080	0.0086	0.0080
MAE	0.030	0.031	0.031	0.029	0.027	0.029
LRBFDQ						
R_{13}						
$RMSE$	0.0080	0.0036	0.0076	0.016	0.020	0.016
MAE	0.30	0.13	0.29	0.61	0.74	0.60
R_9						
$RMSE$	0.0076	0.0044	0.0076	0.059	0.054	0.059
MAE	0.29	0.17	0.29	2.24	2.03	2.24
CSRBF						
$RMSE$	0.70	0.32	0.35	0.46	0.38	0.49
MAE	1.48	0.18	0.67	0.81	0.92	0.91
Global − MQ						
$RMSE$	0.49	0.71	1.01	0.63	1.0	1.48
MAE	1.19	1.51	1.76	1.06	2.33	2.74

Table 2: Example 4, natural convection: Comparison of the average Nusselt number between the proposed method and some other methods for Ra in the range of 10^4 to 10^6.

Ra	10^4	5×10^4	10^5	5×10^5	10^6
			Nu		
Proposed method	3.23	4.04	4.88	7.68	9.38
1D IRBF [36]	3.22	4.04	4.89	7.43	8.70
FVM [29]	3.24		4.86		8.90
MQ-DQ [37]	3.33		5.08		9.37

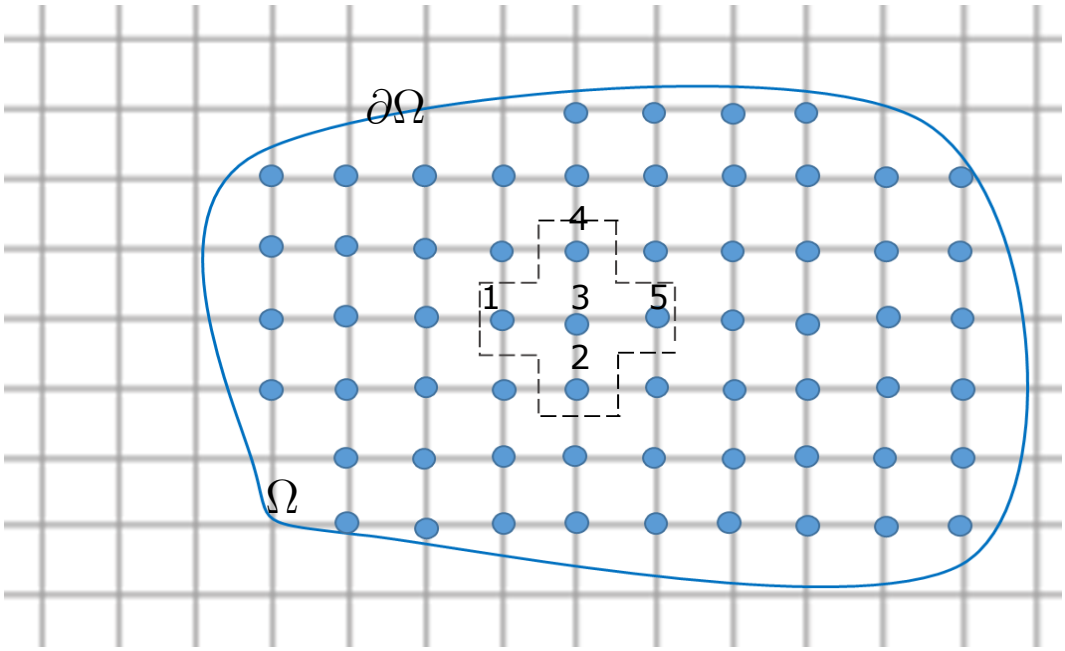

Figure 1: Domain of interest and its Cartesian-grid representation.

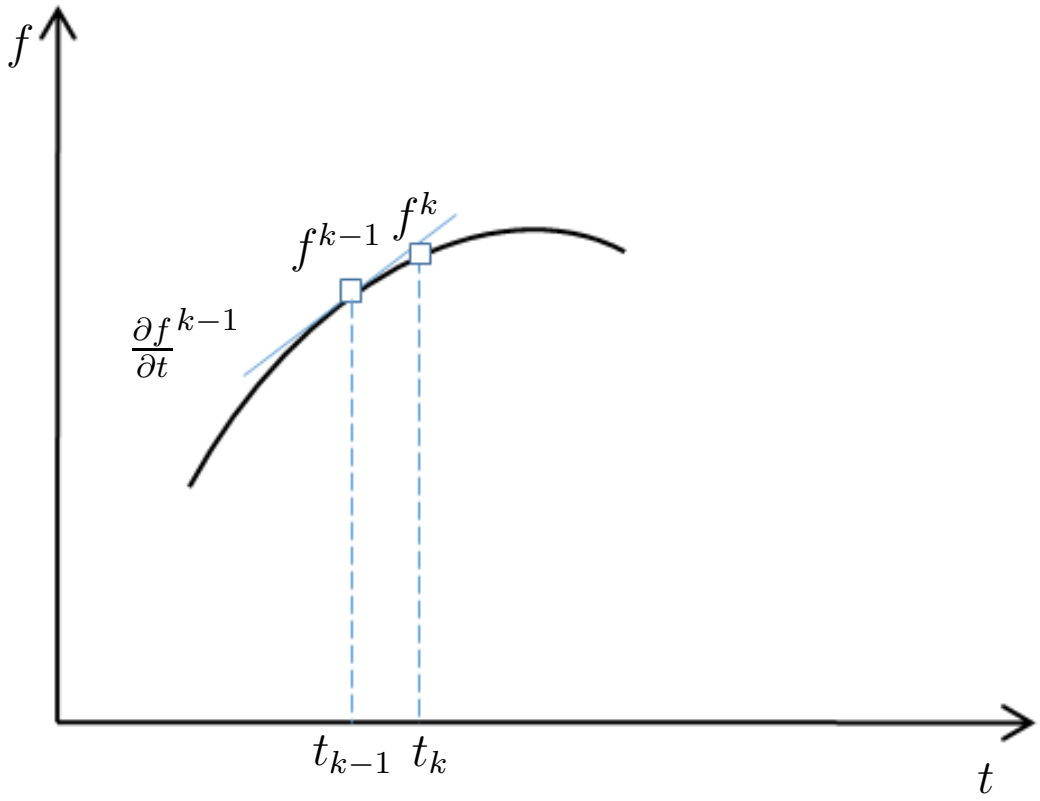

Figure 2: Information used to approximate the time derivative term on a time step includes the variable values at t_{k-1} and t_k, and the derivative value at t_{k-1}.

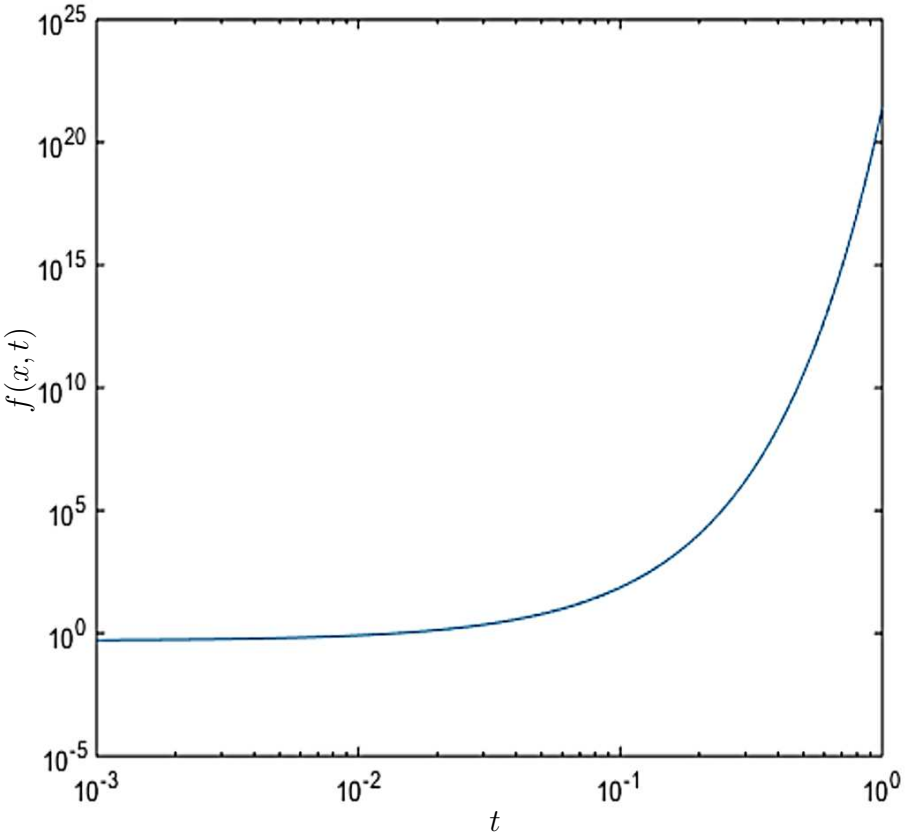

Figure 3: Example 1.1, parabolic PDE: Variation of $f(x,t)$ with time at $x = 0.5$.

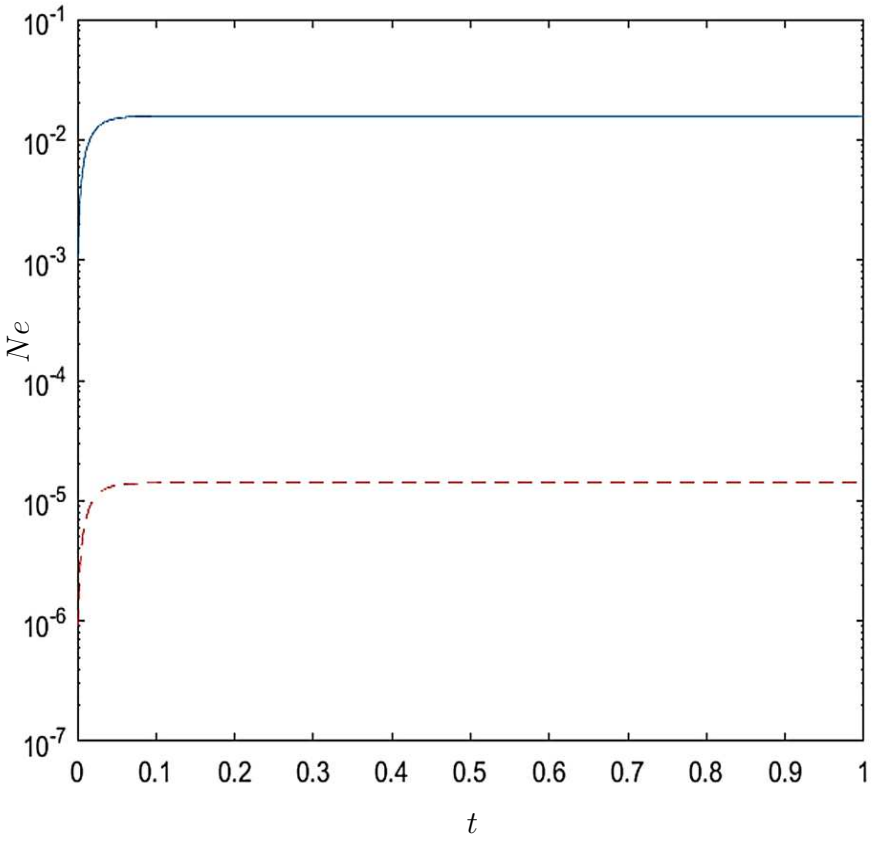

Figure 4: Example 1.1, parabolic PDE, spatial compact IRBF stencils, $\Delta t = 10^{-3}$: Comparison of the solution accuracy between the FD ('$-$') and IRBF ('- -', $\beta_t = 18$) time discretisations.

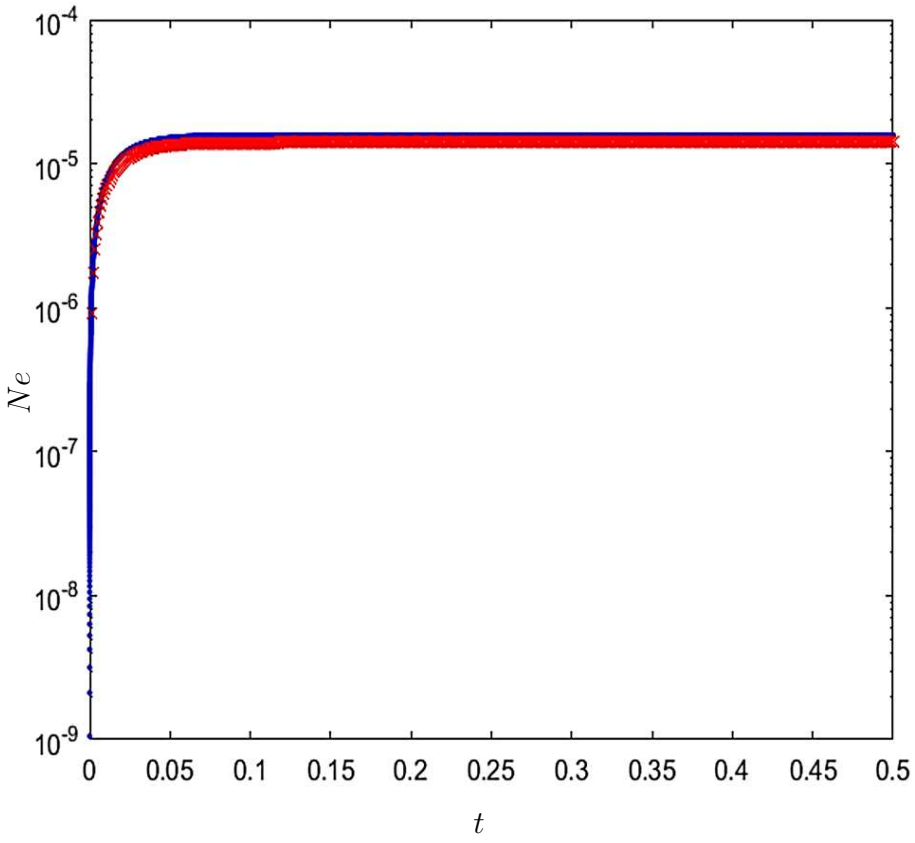

Figure 5: Example 1.1, parabolic PDE, spatial compact IRBF stencils: Comparison of the solution accuracy between the FD ('$\cdot$', $\Delta t = 10^{-6}$) and the IRBF ('$\times$', $\Delta t = 10^{-3}$, $\beta_t = 18$) time discretisations.

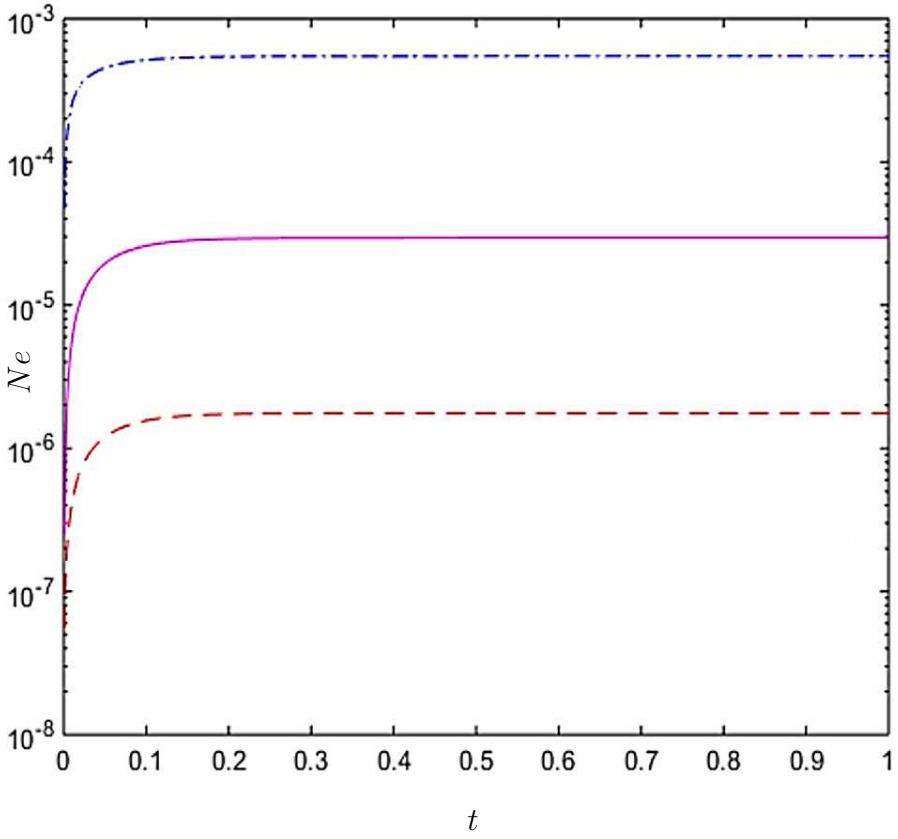

Figure 6: Example 1.2, parabolic PDE, rectangular domain, $\Delta t = 10^{-3}$: Numerical errors obtained by the FD time-FD space ('$\cdot-$'), IRBF time-FD space ('$-$') and IRBF time-IRBF space ('- -') discretisations.

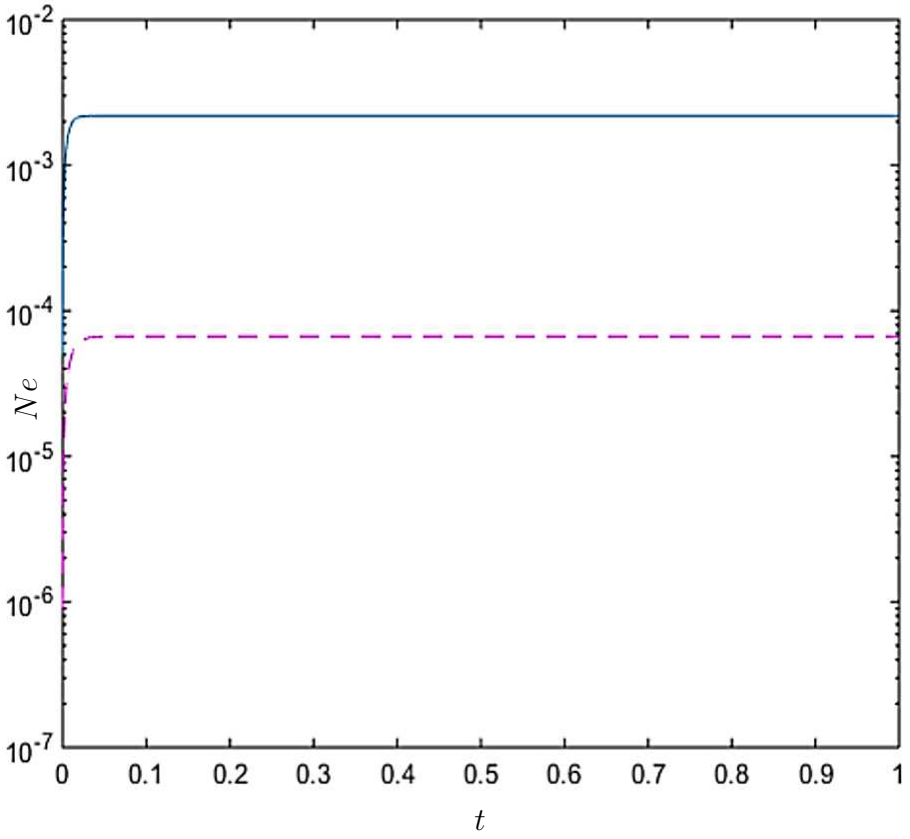

Figure 7: Example 1.2, parabolic PDE, non-rectangular domain, spatial compact IRBF stencils, $\Delta t = 10^{-4}$ and $\beta_t = 10$: Numerical errors obtained by the FD time ('$-$') and IRBF time ('- -') discretisations.

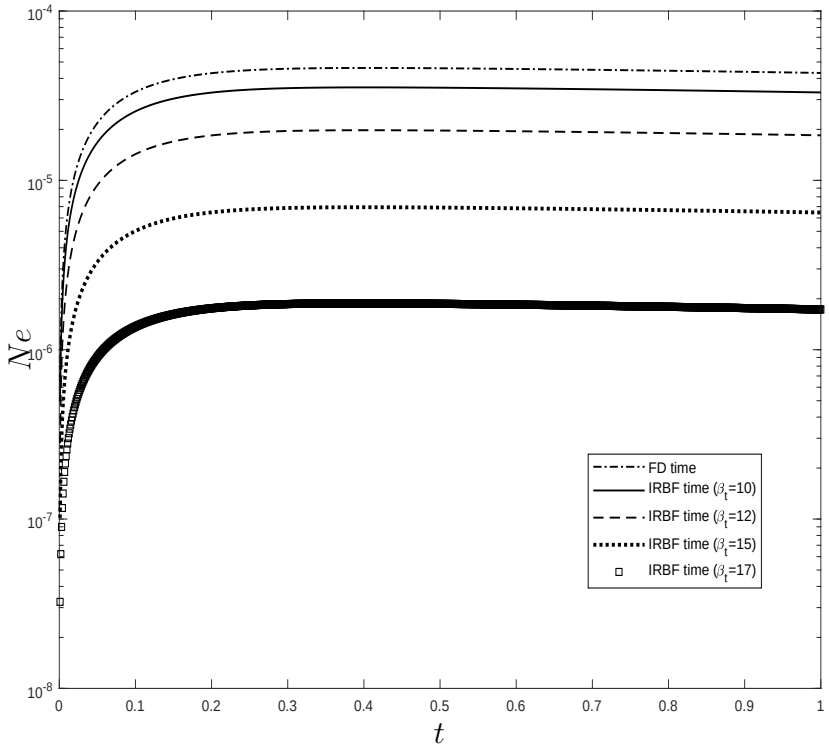

Figure 8: Example 2.1, 1D convection-diffusion equation, $\Delta t = 10^{-3}$: Effect of the temporal RBF width, represented through β_t (β_t= 10, 12, 15, 17), on the IRBF solution accuracy. Results by the conventional FD method are also included.

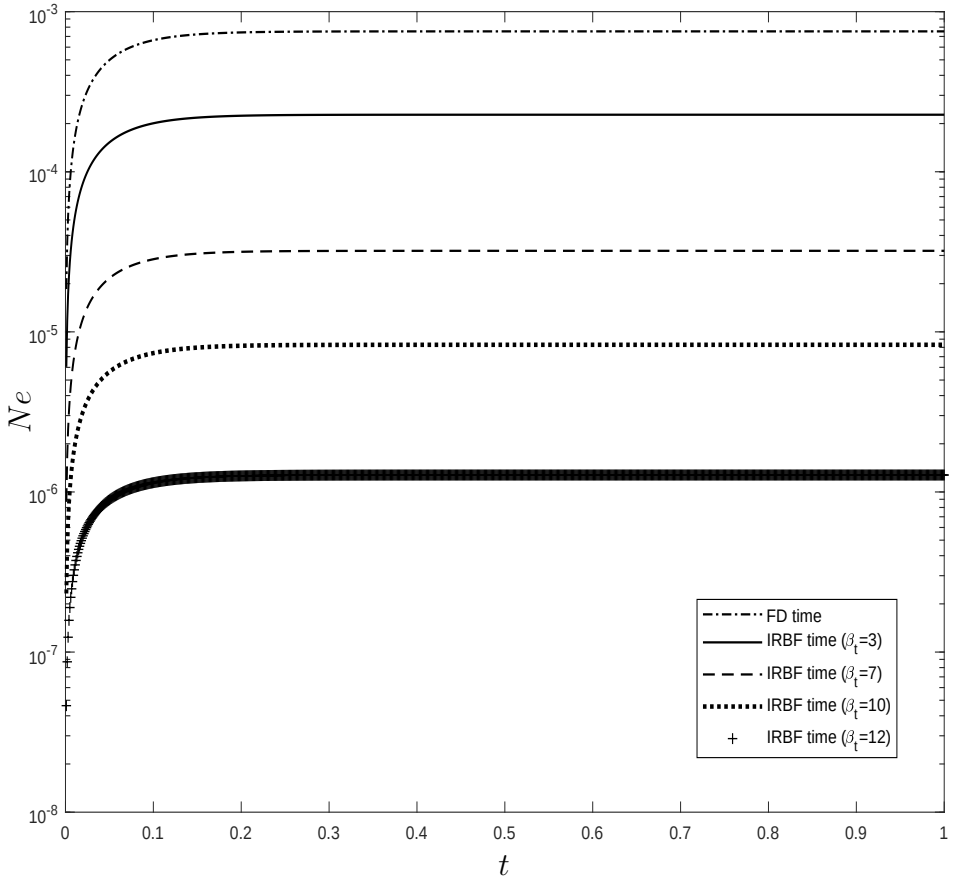

Figure 9: Example 2.2, 2D convection-diffusion equation, $\Delta t = 10^{-3}$: Effect of the temporal RBF width, represented through β_t (β_t= 3, 7, 10, 12), on the IRBF solution accuracy. Results by the conventional FD method are also included.

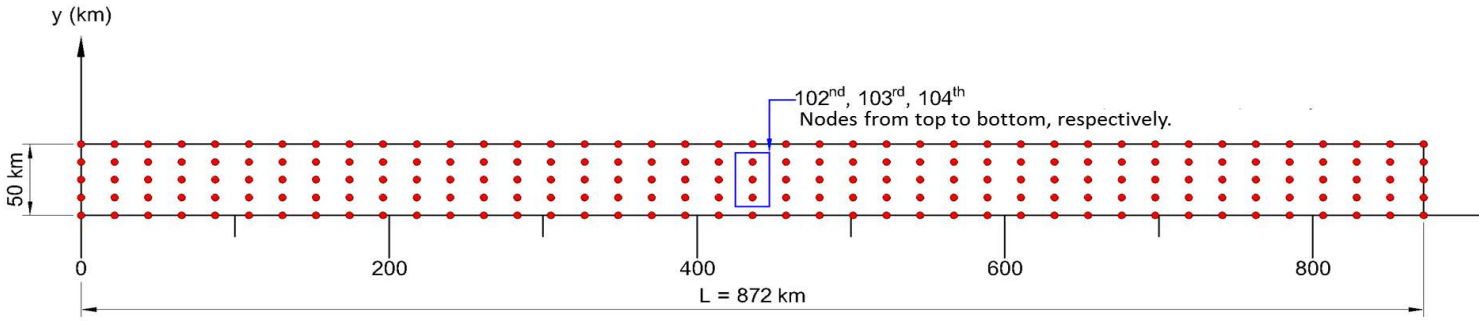

Figure 10: Example 3, shallow water flows: A rectangular channel and its Cartesian grid of 41×5. Numerical results obtained are compared at nodes 102, 103 and 104.

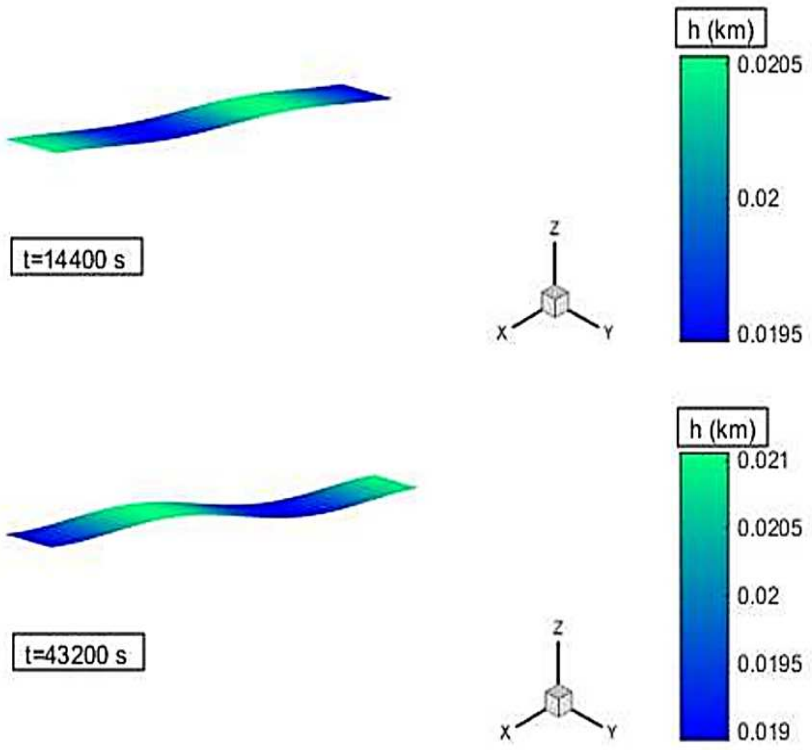

Figure 11: Example 3, shallow water flows: Water surfaces at $t = 14440\ s$ and $t = 43200\ s$ by the proposed method.

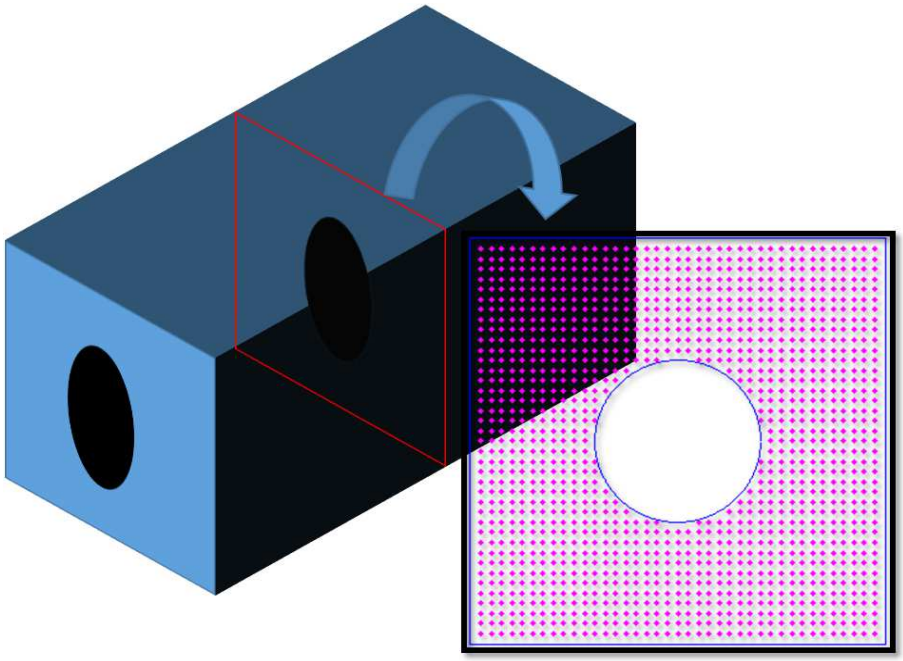

Figure 12: Example 4, natural convection: A domain of analysis and its Cartesian grid.

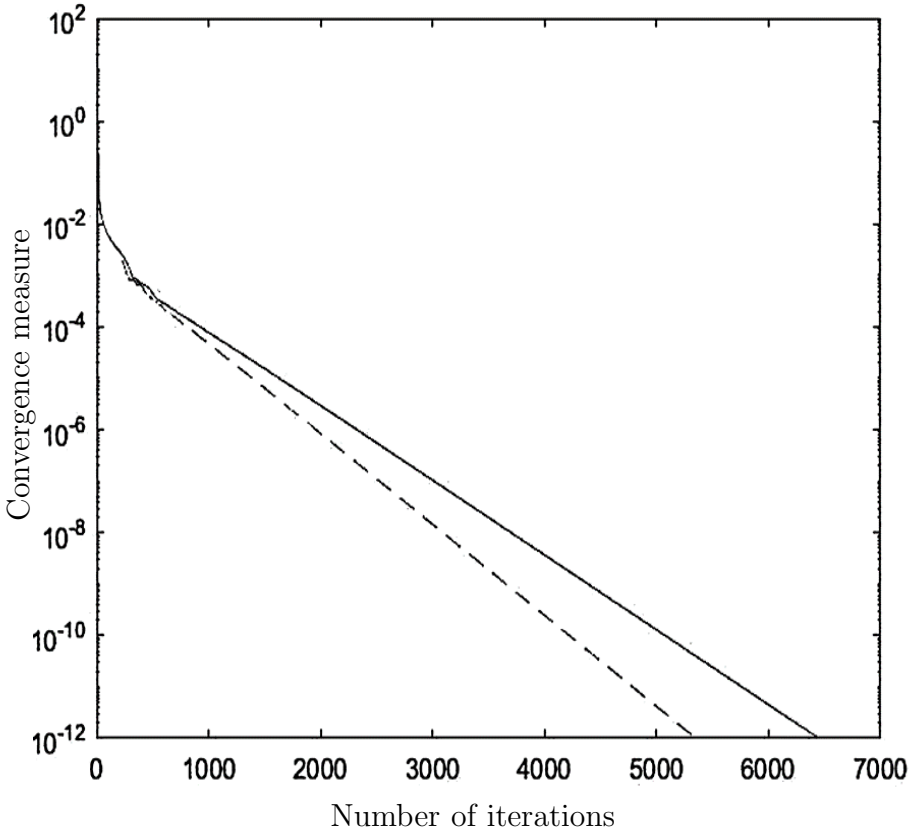

Figure 13: Example 4, natural convection, spatial compact IRBF stencils, $\Delta t = 0.02$ (IRBF) and $\Delta t = 0.014$ (FD), $Ra = 10^5$: The IRBF approximation with respect to time can work with a larger time step and its convergence ('$--$') is seen to be faster than that of the conventional FD one ('-').

$Ra = 10^4$

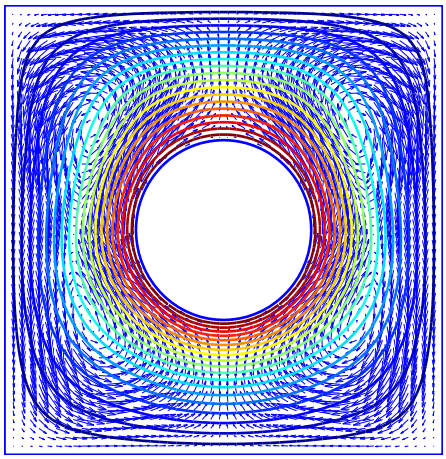

$Ra = 10^5$

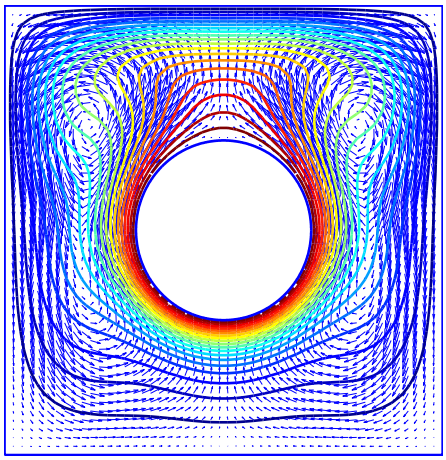

$Ra = 10^6$

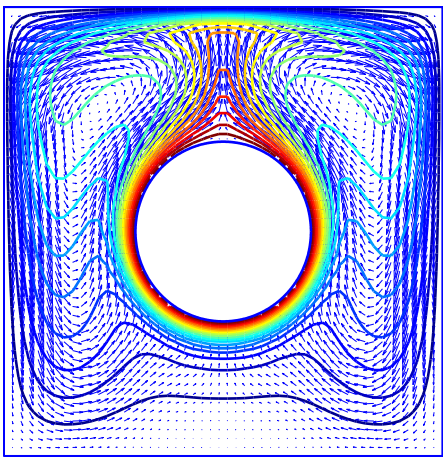

Figure 14: Example 4, natural convection: velocity vector field and contour plots of the temperature for several values of Ra by the proposed method.